Nanoscale Advances

ROYAL SOCIETY OF CHEMISTRY

PAPER

View Article Online
View Journal | View Issue

Cite this: *Nanoscale Adv.*, 2022, **4**, 182

Preparation of $SrTiO_3$ nanocubes by CO_2 laser vaporization (LAVA) and hydrothermal maturation†

Lenka Müller, Philipp Hornig, Janet Grabow and Frank A. Müller*

Received 14th September 2021
Accepted 7th November 2021

DOI: 10.1039/d1na00685a

rsc.li/nanoscale-advances

$SrTiO_3$ is of particular interest for numerous applications such as photocatalytic water splitting, as an electrode material for thermoelectrics or as piezoceramics for sensors. Here we report on an advanced CO_2 laser vaporization (LAVA) method for the production of faceted, single-phase $SrTiO_3$ nanoparticles with an average particle size of 35 nm. Starting from a coarse $SrTiO_3$ raw powder, spherical $SrTiO_3$ nanoparticles were obtained by a laser-induced gas-phase condensation process. The composition of the nanoparticles corresponds to that of the starting powder, as XRD and FT-IR measurements show. Further hydrothermal treatment at 275 °C for 4 hours leads to the formation of faceted nanocubes with increasing crystallite size, as demonstrated by TEM, HR-TEM and XRD measurements. During a final washing step in 0.1 M HCl, $SrCO_3$ impurities were dissolved and thus single-phase $SrTiO_3$ nanocubes were successfully obtained, as shown by FT-IR, XRD and TEM analyses. The presented process facilitates the production of single-phase, highly crystalline $SrTiO_3$ nanopowders in sufficient quantities for subsequent use in a variety of applications, in particular for hydrogen production by photocatalytic water splitting.

Introduction

With the growth of the population and the associated increase in energy demand, the search for sustainable energy sources that reduce the dependence on fossil fuels and minimize environmentally harmful emissions is also intensifying. Hydrogen seems to be an attractive energy carrier that causes almost no emissions at the end user's site.[1–4] Among the various methods of hydrogen production from renewable and non-renewable sources, water splitting has been of particular interest in recent decade.[5–7] Fujishima and Honda discovered that water can be decomposed into H_2 and O_2 using titanium dioxide as a catalyst.[8] This so-called photocatalytic water splitting is a complex multi-electron transfer process that uses specific spectral ranges of sunlight. Besides the intensively studied titanium dioxide,[9–15] certain perovskites,[2,16–18] which are composed of ternary oxides of the structure ABO_3, where A is usually a group I or II element and B is usually a transition metal, are of particular interest. Among them, strontium titanate, $SrTiO_3$, with its stable cubic structure at ambient temperature and pressure, high melting point (2080 °C) and chemical stability, seems to be a promising photocatalyst as it has a more negative conduction band edge compared to TiO_2.[1,2,4,16,19–21] Generally, the activity of heterogeneous catalysts is affected by their crystallinity, surface area, particle size and the purity of the crystal phase. It was described that the morphology, crystallinity and size of $SrTiO_3$ particles depend not only on the starting material but also on the processing route.[2] Commonly, $SrTiO_3$ is processed by solid-state reactions of oxides/carbonates such as $SrO/SrCO_3$ and TiO_2.[22–24] This processing method requires high temperatures for extended calcination times, and thus significantly influences the microstructure and properties of the final compound. Subsequent conventional ball milling to obtain a fine-grained powder is likely to introduce impurities. Therefore, other methods for the fabrication of $SrTiO_3$ have been investigated, such as sol–gel techniques,[25–27] co-precipitation,[28,29] microwave-assisted processing,[30] combustion methods,[31–33] and hydrothermal processes.[2,19,34–40] A review of the methods for the synthesis of $SrTiO_3$ published in the literature in the last decade is given by Phoon *et al.*[2] In addition, a large specific surface area is advantageous for photocatalysts, suggesting the use of nanoparticles with their high surface-to-volume ratio. It is known that chemically pure, crystalline, oxide nanoparticles with a narrow size distribution can be prepared from coarse raw powders using CO_2 laser vaporization (LAVA).[41–46] In this work, the LAVA method was applied to produce spherical strontium titanate nanoparticles, which were subsequently hydrothermally treated to obtain faceted $SrTiO_3$ nanocubes.

Materials and methods

Samples processing

Commercially available $SrTiO_3$ powder (purity: 99.9%, particle size: 2–3 μm, Biotain Hong Kong Co., Limited) was used as a starting material (sample labeling: STO-raw). The LAVA

Otto-Schott-Institute of Materials Research (OSIM), Friedrich-Schiller-University of Jena, Löbdergraben 32, 07743 Jena, Germany. E-mail: frank.mueller@uni-jena.de

† Electronic supplementary information (ESI) available. See DOI: 10.1039/d1na00685a

method was applied to prepare the $SrTiO_3$ nanoparticles.[41] Briefly, a CO_2 laser beam is focused on the surface of the starting powder that is located in a rotating container ring. Due to the absorption of the intense laser radiation, the raw powder heats up, vaporizes and forms a plasma above the beam focus, which cools down rapidly as it expands into the process gas at normal pressure. Consequently, ultrafine particles are formed by gas phase condensation. Finally, the desired nanopowder is obtained, which generally has the same chemical composition as the target raw powder.[41] Pulsed CO_2 laser radiation (wavelength: 10.59 μm, pulse length: 1 ms, pulse repetition frequency: 200 Hz, average radiation power: 730 W, pulse peak power: 3.5 kW, focus diameter: 1 mm) and air as process gas (flow rate in the vaporization zone: 2 $m^3\ h^{-1}$, total flow rate: 14.5 $m^3\ h^{-1}$) were used for the preparation of the nanoparticles (sample labeling: STO-LV). Pulsed laser radiation was used to reduce the particle size and the width of their distribution, and to minimize the number of primary particles firmly bound by solid state bridges.[43]

The STO-LV nanoparticles (1.5 g) were suspended in 200 ml distilled water and further treated in a hydrothermal reactor (4560 Mini Reactor 600 ml, Parr Instruments, USA) under stirring at 275 °C and 38 bar for 4 h and then cooled to room temperature. Subsequently, the suspension was centrifuged at 5000 rpm (Megafuge 1.0, Heraeus, Germany) and the powder was finally dried at 70 °C (sample labeling: STO-LV-hy).

The dried STO-LV-hy nanoparticles were washed in 0.1 M HCl (Carl Roth, Germany) for 20 min and subsequently centrifuged at 6000 rpm for 3 min (ThermoFisher SCIENTIFIC, Heraeus Multifuge X1R, Germany). The centrifugate was then washed several times with distilled water and finally dried at 60 °C for 24 hours (sample labeling: STO-LV-hy-HCl).

An overview about sample labeling and corresponding processing steps is shown in Table 1.

Characterization

Transmission electron microscopy (TEM) (Zeiss EM 900, Oberkochen, Germany) at an accelerating voltage of 80 kV and a maximum magnification of 250 000 was used to investigate the morphology of the nanoparticles after LAVA and hydrothermal processing. For this purpose, a small amount of the nanopowder was ultrasonically dispersed in ethanol and dropped on a TEM grid (circular perforated carbon film on copper mesh, Quantifoil Micro Tools, Groβloebichau, Germany).

The particle size distribution was determined from TEM micrographs by measuring the diameters of more than 1400 primary nanoparticles using the Gatan Digital Micrograph software (Pleasanton, CA, USA) assuming a spherical shape of the particles.[47] From these values, the percentage density distributions of the particle diameters on a number basis q_0, on diameter basis q_1 and on surface basis q_2 were calculated. The measured distribution was fitted with a logarithmic normal distribution in order to obtain the corresponding geometric mean particle diameters $\mu_g(q_0)$, $\mu_g(q_1)$ and $\mu_g(q_2)$, respectively. The cumulative distribution of the particle diameters Q_0 was fitted with a sigmoid function to obtain the characteristic particle diameters d_{10}, d_{50}, and d_{90}.[47] The specific surface area S_{TEM} of the nanopowder sample was calculated from $\mu_g(q_2) = 36.9 \pm 0.8$ nm using the density ($\rho = 5.12$ g cm^{-3}) of the commercial $SrTiO_3$ powder and by assuming spherical particles.[48]

A high-resolution transmission electron microscope (HR-TEM) (JEOL JEM-ARM200F NEOARM, JEOL GmbH, Germany, accelerating voltage of 200 kV) was used to obtain structural information of the powder at the atomic level and to determine lattice plane spacings. The images were taken with a 4K-CMOS-camera (GATAN OneView, USA). The frequency distribution of the intensities was determined from 2048 px × 2048 px HR-TEM images using the Fast Fourier Transform (FFT) function of the camera software (DigitalMicrograph version 3.43.3213.0, Gatan Inc., USA).

The starting STO-raw powder as well as STO-LV, STO-LV-hy and STO-hy-HCl samples were characterized by X-ray powder diffraction analysis (XRD) using CuKα radiation ($\lambda = 0.15405$ nm) at an accelerating voltage of 30 kV and a beam current of 10 mA (Miniflex 300, Rigaku, Japan). Data were recorded with a sample rotation in the range of 5–75° 2θ, a step width of 0.02° and a scan rate of 1° min^{-1}. Furthermore, mean crystallite sizes D were calculated from the corresponding diffractograms using Scherrer's eqn (1) with a shape factor $K = 1.107$ (the reflexes were fitted by Gaussian function), wavelength λ, $FWHM_{200}$ the full-width-at-half-maximum of the (200) reflex and θ the angle of this diffraction line.[49–51]

$$D = \frac{K\lambda}{\cos\theta\sqrt{FWHM_{200}{}^2 - FWHM_{LaB_6}{}^2}} \quad (1)$$

The $FWHM_{200}$ was corrected for the instrumental broadening $FWHM_{LaB6}$ determined from the measurement of a LaB_6 standard material.

Fourier transform infrared (FT-IR) spectra were measured using the KBr technique in the range from 4000 to 400 cm^{-1} at a resolution of 4 cm^{-1} at 32 scans (Alpha-T, Bruker, Germany). Approximately 1 mg of the samples was mixed with 300 mg of dry KBr powder and ground using an agate mortar and pestle. The resulting mixture was uniaxial pressed into transparent pellets with a diameter of 13 mm using a pressing tool (PW 20,

Table 1 Sample labeling and corresponding processing steps

Sample labeling/process step	STO-raw	STO-LV	STO-LV-hy	STO-LV-hy-HCl
LAVA processing	—	Yes	Yes	Yes
Hydrothermal maturation	—	—	Yes	Yes
Acid etching	—	—	—	Yes

Carl Zeiss, Jena, Germany) and applying a force of up to 50 kN (P/O/Weber Laborpresstechnik, Remshalden, Germany). All sample data were normalized to the most intense signal in each case.

Results and discussion

$SrTiO_3$ raw powder (STO-raw)

XRD analysis of the starting powder (Fig. 1) shows sharp reflections at 22.8°, 32.4°, 40°, 46.5°, 52.4°, 57.8° and 67.8° 2θ that can be assigned to $SrTiO_3$ (JCPD card-no. 35-0734). According to JCPD card-no. 05-0418 diffraction lines of $SrCO_3$ can be found at 25.2°, 25.8°, 31.5°, and 36.2° 2θ. Moreover, the small reflexes at 27.5° and 54.4° 2θ correspond to TiO_2 (JCPD card-no. 87-0710) with the tetragonal structure of rutile. The chemical bonding characteristics of the sample were measured using FT-IR spectra shown in Fig. 2.

The low-frequency bands detected in the STO-raw powder, centred at 588 and 434 cm^{-1}, are typical of metal–oxygen stretching in titanate compounds and correspond to Ti–O, Ti–O–Ti, Sr–O and Sr–Ti–O vibrations.[52–54] Beyond, the broad and intense band between 900 and 400 cm^{-1} with a maximum at 588 cm^{-1} can be assigned to Ti–O and Ti–O–Ti stretching and bending vibrations in TiO_2.[55] In addition, the vibration at 1460 cm^{-1} can be assigned to $(CO_3)^{2-}$.[56] The FT-IR analyses of the STO-raw powder correspond with the XRD measurement, where strontium titanate, strontium carbonate and rutile were detected.

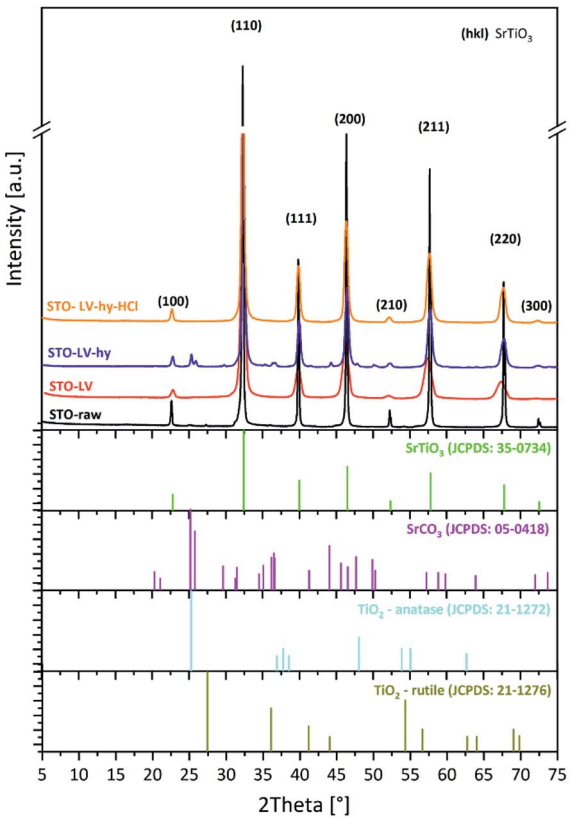

Fig. 1 X-ray diffraction analyses of the starting $SrTiO_3$ powder (STO-raw) compared with those after LAVA processing (STO-LV), LAVA processing and hydrothermal treatment (STO-LV-hy) as well as after LAVA processing, hydrothermal treatment and subsequent acid etching (STO-LV-hy-HCl).

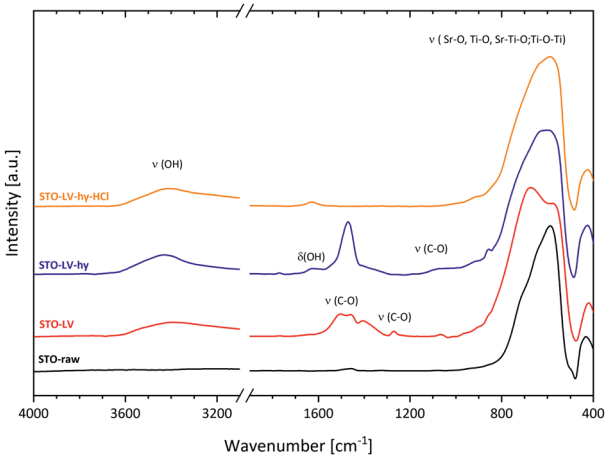

Fig. 2 FT-IR analysis of the $SrTiO_3$ starting powder (STO-raw) compared with those after LAVA processing (STO-LV), LAVA processing and hydrothermal treatment (STO-LV-hy) as well as after LAVA processing, hydrothermal treatment and subsequent acid etching (STO-LV-hy-HCl).

$SrTiO_3$ raw powder processed by laser vaporization (STO-LV)

The $SrTiO_3$ nanoparticles were produced by the LAVA process under air atmosphere using pulsed CO_2 laser radiation in a continuous process.[41,47] The production rate of the nanoparticles was 18.1 g h^{-1}. The LAVA nanoparticles are predominantly spherical in shape and only slightly agglomerated by weak van der Waals forces, as the overview TEM micrograph of the sample shows (Fig. 3a). The average particle diameter d_{50} is 23.7 nm and the distribution width d_{90}–d_{10} is 32.13 nm. The geometric mean diameter on number basis $\mu_g(q_0)$ and on diameter basis $\mu_g(q_1)$ is 26.5 ± 1.0 and 31.0 ± 0.9 nm, respectively (Fig. 3b). The specific surface area S_{TEM} calculated from the particle size distribution is 31.8 m^2 g^{-1}.

HR-TEM images (Fig. 3c and d) confirm the crystalline structure of the nanospheres. The *d*-spacing calculated from the HR-TEM image in Fig. 3d is 0.19 and 0.22 nm, respectively. This is only slightly different from that of the (200) (0.195 nm) and (111) (0.225 nm) planes of $SrTiO_3$ and could be explained by the formation of vacancies during the LAVA process leading to negligible lattice changes.

The processing of the starting powder by LAVA causes a broadening of the $SrTiO_3$ diffraction lines (Fig. 1), which indicates a more nanocrystalline structure compared to the starting powder. However, the diffraction lines can still be assigned to the cubic perovskite structure of $SrTiO_3$ (JCPD card-no. 35-0734). The mean crystallite size of the (200) reflex calculated from Scherrer's equation is 12 nm for the STO-LV and 136 nm for the STO-raw powder, respectively. Furthermore, no secondary phase was detected in the STO-LV sample using X-ray diffraction.

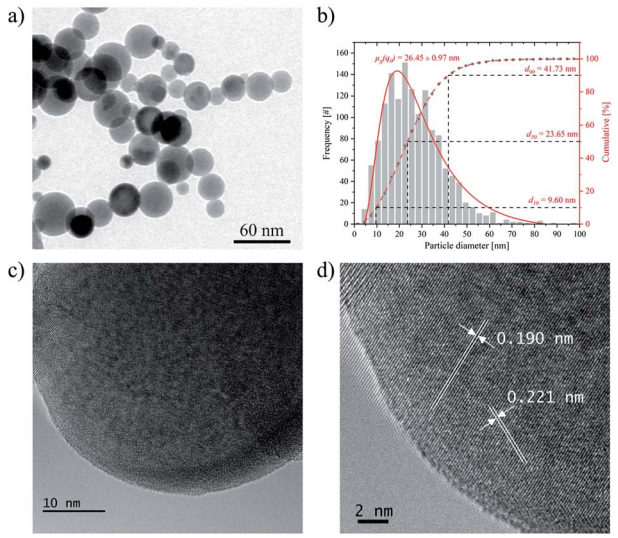

Fig. 3 (a) TEM micrograph of STO-LV powder (overview), (b) TEM-derived particle size distribution of STO-LV: frequency-based nanoparticles diameter distribution (log normal (—) and cumulative (---) distribution) with the geometric mean diameter $\mu_g(q_0)$ and the characteristic diameters d_{10}, d_{50}, and d_{90}, (c and d) HR-TEM images of STO-LV.

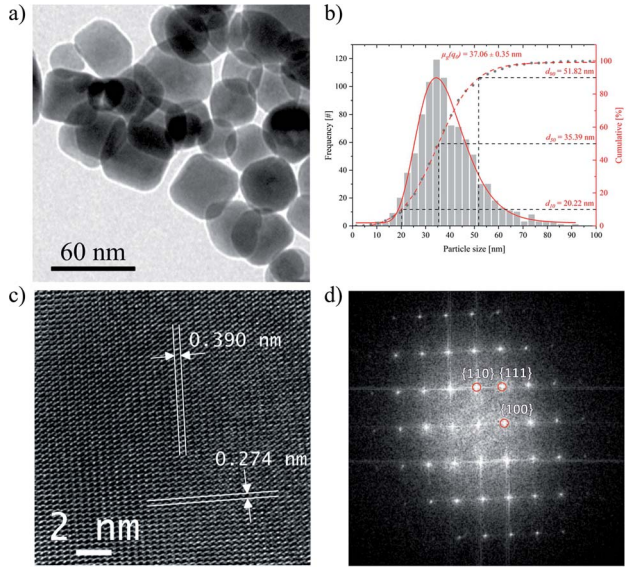

Fig. 4 (a) TEM micrograph of STO-LV-hy nanoparticles (overview), (b) TEM-derived particle size distribution of STO-LV: frequency-based nanoparticles diameter distribution (log normal (—) and cumulative (---) distribution) with the geometric mean diameter $\mu_g(q_0)$ and the characteristic diameters d_{10}, d_{50}, and d_{90}, (c) HR-TEM image, (d) indexed FFTs from the corresponding selected area.

After LAVA processing, the H_2O adsorbed on the surface can be detected in STO-LV sample using FT-IR (Fig. 2) as the broad stretching vibration of hydroxyl group in H_2O appeared at 3400 cm^{-1}. Furthermore, the absorptions at 1065, 1270, 1405, 1458 and 1502 cm^{-1} are due to vibrations of $(CO_3)^{2-}$ and can thus be attributed to $SrCO_3$, which is also produced along with $SrTiO_3$.[52,56–58] However, $SrCO_3$ was not found by X-ray diffraction analysis which is probably due to its low content and/or low crystallinity and thus relatively weak diffraction intensities. EDX analyses of TEM-samples could not be used to prove the presence of carbonate, since the copper mesh grids were covered with carbon film. Splitting of the broad vibration ranging from 900 to 400 cm^{-1} into a doublet may be attributed to the decrease in the symmetry of the titanate structure unit (TiO_6 octahedra). This assumption can be supported by the HR-TEM analysis (Fig. 3d), which shows a slightly smaller (001) lattice plane spacing in $SrTiO_3$, probably due to lattice vacancies.[59]

$SrTiO_3$ raw powder processed by laser vaporization and hydrothermal maturation (STO-LV-hy)

From the TEM analyses (Fig. 4a) of hydrothermally treated STO-LV nanoparticles, it becomes evident that the treatment affects the particle shape. Applying pressure and temperature promotes the development of well-defined facets and the formation of cubic nanoparticles of uniform size and regular morphology (Fig. 4a). The average particle size d_{50} is 5.4 nm and the distribution width d_{90}–d_{10} is 31.6 nm. The geometric mean diameter on number basis $\mu_g(q_0)$ is 37.06 ± 0.35 nm (Fig. 4b).

Representative HR-TEM micrograph is shown in Fig. 4c. Lattice planes are visible throughout the entire particles. The lattice spacings of 0.390 nm and 0.274 nm are consistent with the values of the (001) and (110) planes of $SrTiO_3$, respectively. The fast Fourier transforms (Fig. 4d) show that lattice fridges in the region correspond to (110), (111) and (100) planes of $SrTiO_3$.

The XRD results for STO-LV-hy powder in Fig. 1 illustrate that the diffraction lines fit well to those of $SrTiO_3$ (JCPD card-no. 35-734) with a standard cubic perovskite structure (space group *Pm3m*).

The hydrothermal treatment leads to a decrease of the width at half maximum intensity of the diffraction lines indicating an increase in the crystallite size of the (200) reflex to 20.5 nm according to Scherrer's equation. According to the literature[2,19] the composition, size and morphology of the particles can be adjusted or even controlled by varying some physical and chemical parameters such as temperature, concentration, pH and solvent composition. Furthermore, it has been shown that different precursors and solvents influence the shape, size distribution and crystallinity of $SrTiO_3$. In our case, however, we did not synthesise $SrTiO_3$ from precursors (*e.g.* TiO_2 or $TiCl_4$), but used the hydrothermal reactor only for maturation (ageing). An extended maturation time of up to 8 hours and a higher temperature of up to 300 °C did not change the particle or crystallite size.

However, $SrCO_3$ (JCPD card-no. 05-0418) is observed in this XRD pattern with the two strongest lines at 25.2° (111) and 25.8° (021) 2θ, probably as a by-product of the hydrothermal reaction.[36,60–62] Furthermore, anatase TiO_2 (JCPD card-no. 21-1271) with its most intense reflexes at 25.2° (101) and 48° (200) 2θ cannot be excluded, as they partially overlap with those of strontium carbonate.

After hydrothermal treatment, a new band at 1630 cm^{-1} and a broad band around 1100 cm^{-1} were detected using FT-IR (Fig. 2) in the STO-LAVA-hy sample representing the bending vibration of the hydroxyl group in H_2O and a symmetric stretching of C–O in $(CO_3)^{2-}$, respectively.[56] This analysis confirms the results obtained by XRD where $SrCO_3$ was detected.

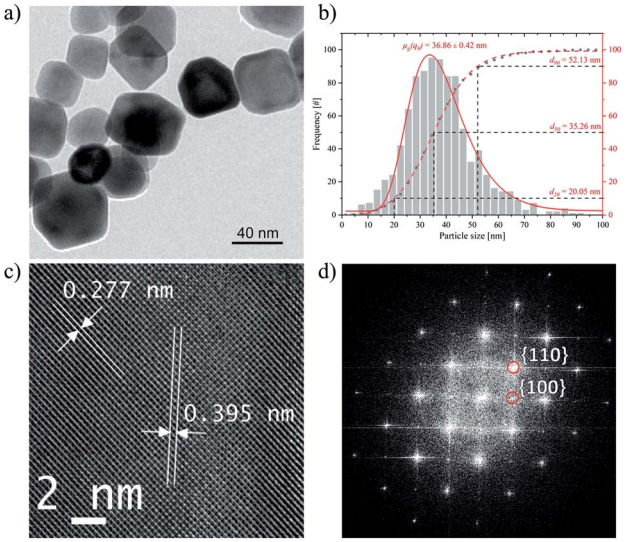

Fig. 5 (a) TEM micrograph of STO-LV-hy-HCl nanoparticles (overview), (b) TEM-derived particle size distribution of STO-LV-hy-HCl: frequency-based nanoparticles size distribution (log normal (—) and cumulative (- - -) distribution) with the geometric mean diameter $\mu_g(q_0)$ and the characteristic diameters d_{10}, d_{50}, and d_{90}, (c) HR-TEM image, (d) indexed FFTs from the corresponding selected area.

$SrTiO_3$ raw powder processed by laser vaporization, hydrothermal maturation and acid etching (STO-LV-hy-HCl)

Finally, the STO-LAVA-hy powder was washed with 0.1 M HCl in order to eliminate $SrCO_3$.

Consequently, all reflexes match well with the pattern of cubic $SrTiO_3$ (JCPD card-no. 35-0734) and no other diffraction lines of any other phases can be detected, indicating that the powder consist of pure strontium titanate. The narrow XRD reflexes in Fig. 1 indicate that the nanoparticles are well crystalline with a $D_{(200)}$ crystallite size of 20.3 nm according to Scherrer's equation. Subsequent acid etching successfully removed the carbonate, which according to FTIR measurements (Fig. 2) of STO-LV-hy-HCl indicates single phase $SrTiO_3$ and is confirmed by the XRD results.

TEM analysis (Fig. 5a) revealed that acid etching using 0.1 M HCl affects neither the facet shape of the nanoparticles nor their size. The average particle size d_{50} is 35.3 nm and the distribution width d_{90}–d_{10} is 32.1 nm. Higher concentrations (1 M HCl) and longer etching times (up to 60 min) lead to partial dissolution of the particles.

The geometric mean diameter on number basis $\mu_g(q_0)$ is 36.9 ± 0.4 nm (Fig. 5b). HR-TEM images (Fig. 5c) and FFT (Fig. 5d) show that the crystalline structure has remained virtually unchanged by the etching process.

Temperature and process step-dependent development of $SrTiO_3$ nanocubes

$SrTiO_3$ is of particular interest for numerous applications such as photocatalytic water splitting,[16,20] as an electrode material for thermoelectrics[63] or as piezoceramics for sensors.[64] For example, Takata *et al.* recently demonstrated a model system of an almost perfectly efficient catalyst by selectively depositing co-catalysts onto the different crystal facets of single-crystalline $SrTiO_3$ particles with a size of 500 nm[1]. By further reducing the particle size and thus increasing the specific surface area, it should be possible to further increase the efficiency of such particles. However, the possibility of producing high-quality $SrTiO_3$ of this particle size is still lacking. In the present work, we have shown that single-phase faceted $SrTiO_3$ nanoparticles can be successfully prepared by laser vaporization, subsequent hydrothermal maturation at 275 °C for 4 hours and etching in 0.1 M HCl. A comparison of the overall morphology of the nanoparticles after the respective process steps observed by TEM is shown in Fig. S1.† Fig. 6 schematically illustrates the process of nanoparticle formation. In the intense focus of the CO_2 laser, the raw material powder, which consists of $SrTiO_3$ and small amounts of SrO, TiO_2 and $SrCO_3$ (Fig. 1 and 2), is vaporized and transferred into a plasma. In the plasma, the ions are present in the same ratio as in the starting material, with the addition of components of the process gas (in this case, air). Thus, overall, the Sr : Ti : O ratio is about 1 : 1 : 3. In the process gas stream, the plasma cools down rapidly until nanoscale

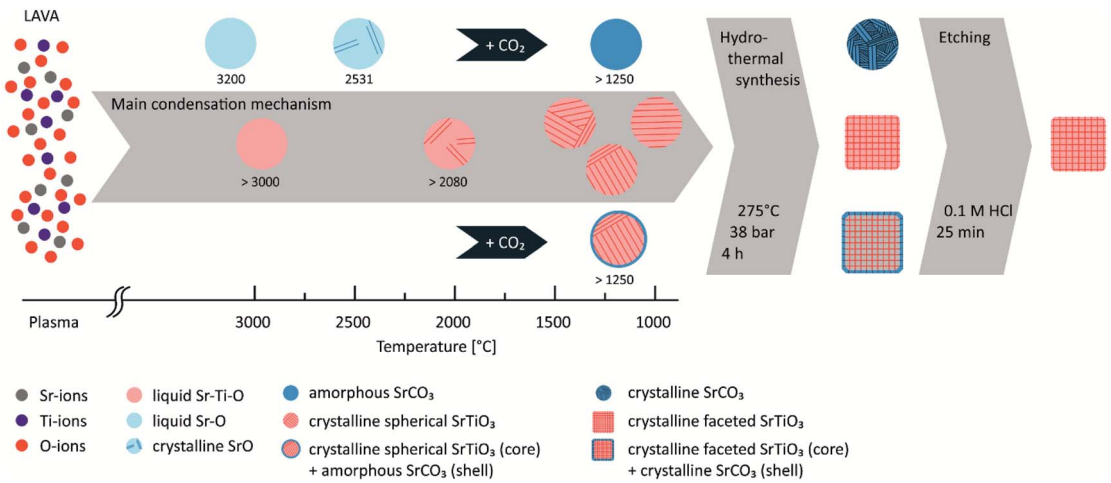

Fig. 6 Schematic illustration of the temperature and process step-dependent development of $SrTiO_3$ nanocubes.

droplets of $SrTiO_3$ composition are formed when the highest vaporization temperature of the components under consideration for condensation is reached (in this case > 3000 °C for $SrTiO_3$).[65] In addition, the formation of liquid SrO and TiO_2 droplets can occur to a much lesser extent upon further cooling below the respective condensation temperature of 3000 °C and 2972 °C.[66,67] When the temperatures fall below the corresponding melting temperatures, SrO crystallizes at 2430 °C,[66] $SrTiO_3$ at 2080 °C (ref. 65) and TiO_2 at 1843 °C.[67] Even before this, however, SrO and TiO_2 droplets can coalesce and crystallize together as $SrTiO_3$. At the same time, carbon can be incorporated into the developing particles during the condensation process or form $SrCO_3$ at temperatures below 1200 °C (ref. 68) by heterogeneous nucleation on the crystalline $SrTiO_3$ particles. EDX analyses of TEM-samples could not be used to detect the presence of carbonate because the copper grids were covered with carbon film. Nevertheless, it has been described that electron beams can damage carbonate (especially calcite) or oxides.[69,70] Under an induced electric field, cations, *e.g.* Ca in $CaCO_3$, can be separated from the $(CO_3)^{2-}$ clusters, forming cation-rich and cation-poor regions or be decomposed into CaO. Therefore, a similar effect cannot be excluded with certainty in the case of $SrCO_3$. It is clear from the XRD and FTIR results (Fig. 1 and 2) that $SrCO_3$ is in amorphous form.

Since nucleation, condensation, coagulation and solidification occur in less than 1 ms due to the rapid quenching from plasma to room temperature, growth by coagulation is prevented.[41,71] Consequently, only nanoscale particles with diameters well below 100 nm are found (Fig. 3b). However, the particles are not single crystalline but consist of several crystal domains, as can be deduced from the discrepancy between particle size ($d_{50} = 23.7$ nm) and domain size ($D_{(200)} = 12$ nm). Furthermore, it was described[45] that some oxides (*e.g.* SiO_2, Al_2O_3) in combination with alkaline-earth metals act as glass formers (vitrificator) when the corresponding melt is quenched. Since no glass former is present in our system, we assume that STO-LV nanoparticles are completely crystalline (Fig. 3d).

As long as crystal growth proceeds under equilibrium conditions, the crystal habit is determined by the symmetry of the corresponding crystal system. However, since the process of particle formation during LAVA proceeds under non-equilibrium conditions,[41] the particles do not exhibit a faceted shape, but remain in the shape of the liquid droplets because the mobility of the atomic components is significantly reduced and the minimization of the surface energy of the crystallite is hindered. This leads to the formation of a less ordered structure, as can be seen from the FT-IR spectra (Fig. 2) by splitting the band associated with the TiO_6 octahedra.

Basically, it has been described that the catalytic properties of $SrTiO_3$ are influenced by its crystallinity, specific surface area, particle size and crystallinity.[2] In particular, well-formed crystal facets seem to be of crucial importance for the efficiency of photocatalytic water splitting.[1,2,19] Static pressure is an alternative to thermo-chemical processes to adjust the crystal structure and physical properties of materials.[72–75] Therefore, the STO-LV powder was hydrothermally treated at 275 °C and 38 bar for 4 h (Fig. 4). During this post-treatment, the $SrTiO_3$ crystals mature *i.e.* domains cluster together and faceted single crystals are formed (Fig. 4a), as shown by the increase in crystallite size $D_{(200)}$ from 12 nm to 20.5 nm according to Scherrer's equation. HR-TEM analyses confirm that lattice planes are pronounced throughout the particle (Fig. 4c), indicating a well-developed crystalline structure of $SrTiO_3$. The development of a more ordered structure can also be concluded from FT-IR measurements (Fig. 2) due to the reversible splitting of the vibration associated with the structural unit TiO_6, which is around 800–400 cm^{-1}. Structural changes of the nanoparticles could be attributed to Ostwald ripening, a process of crystal growth that occurs at the expense of smaller particles dissolving as they are less energetically stable and thus contributing to the growth of larger crystallites.[76–78] This hypothesis is supported by looking at particle and crystallite sizes.

After LAVA processing, the d_{10} particle size and $D_{(200)}$ crystallite size are 9.6 nm and 12 nm, respectively, and increase to 20.2 nm and 20 nm after hydrothermal ripening. Furthermore, the geometry of the particles influences the evaluation of the particle size from the TEM images. The cubes are often twisted, which increases the average value from the two measurement lines and thus the determined particle size. However, the hydrothermal treatment leads to the formation of crystalline $SrCO_3$ (Fig. 1), which was already present in amorphous form in the STO-LV powders between the $SrTiO_3$ domains or as a shell of the particles (Fig. 2). Subsequent etching in 0.1 M HCl dissolves the $SrCO_3$ without affecting the $SrTiO_3$ phase, as confirmed by XRD analysis (Fig. 1). This finally results in single-phase, faceted $SrTiO_3$ nanoparticles (Fig. 5), whose suitability for photocatalytic water splitting but also in thermoelectric or piezoceramic components will be investigated in future work.

Conclusions

Single-phase $SrTiO_3$ nanocubes with high crystallinity were successfully prepared by LAVA processing of a coarse strontium titanate powder followed by a hydrothermal maturation and acid etching. The nanoparticles formed by laser induced gas-phase condensation are spherically shaped with a narrow size distribution and are merely softly agglomerated by weak van der Waals forces. The resulting nanopowder and the raw starting powder are of the same chemical composition. The formation of faceted $SrTiO_3$ nanoparticles was achieved by a subsequent hydrothermal treatment at 275 °C for 4 hours. Subsequent etching in 0.1 M HCl removed $SrCO_3$ impurities and resulted in a single-phase composition of the faceted particles. Owing to the faceted morphology, large specific surface area, single phase composition and high crystallinity, the $SrTiO_3$ nanoparticles are expected to provide significant improvements in a variety of applications, but especially for highly efficient hydrogen production by water splitting. In future work, they will be the basis for reducing the band gap by *in situ* doping as well as for applying co-catalysts for photocatalytic water splitting.

Author contributions

Conceptualization, FAM; writing – original draft preparation, LM; writing – review and editing, FAM, PH, JG, LM; synthesis,

characterisation and data analysis, JG, PH and LM; graphical design, JG; supervision, FAM.

Conflicts of interest

The authors declare no competing financial interest.

Acknowledgements

Financial support from the German Research foundation (DFG, Inst 275/391-1) is gratefully acknowledge. Furthermore, the authors would like to thank D. S. Brauer and S. Ebbinghaus from OSIM-FSUJ for XRD measurements. The assistance with the HR-TEM by K. Freiberg and M. Seyring from OSIM-F UJ is gratefully acknowledged. Also, the access to the TEM at the Electron Microscopy Centre of the University Hospital Jena is appreciated.

Notes and references

1 T. Takata, J. Z. Jiang, Y. Sakata, M. Nakabayashi, N. Shibata, V. Nandal, K. Seki, T. Hisatomi and K. Domen, *Nature*, 2020, **581**, 411–414.
2 B. L. Phoon, C. W. Lai, J. C. Juan, P. L. Show and W. H. Chen, *Int. J. Energy Res.*, 2019, **43**, 5151–5174.
3 T. Takata and K. Domen, *J. Phys. Chem. C*, 2009, **113**, 19386–19388.
4 V.-H. Nguyen, H. H. Do, T. Van Nguyen, P. Singh, P. Raizada, A. Sharma, S. S. Sana, A. N. Grace, M. Shokouhimehr, S. H. Ahn, C. Xia, S. Y. Kim and Q. V. Le, *Solar Energy*, 2020, **211**, 584–599.
5 I. Dincer and C. Acar, *Int. J. Hydrogen Energy*, 2015, **40**, 11094–11111.
6 C. A. Grimes, O. K. Varghese and S. Ranjan, in *Light, Water, Hydrogen: the Solar Generation of Hydrogen by Water Photoelectrolysis*, ed. C. A. Grimes, O. K. Varghese and S. Ranjan, Springer US, Boston, MA, 2008, pp. 35–113.
7 S. Wang, A. Lu and C.-J. Zhong, *Nano Convergence*, 2021, **8**, 4.
8 A. Fujishima and K. Honda, *Nature*, 1972, **238**, 37–38.
9 X. Han, Q. Kuang, M. Jin, Z. Xie and L. Zheng, *J. Am. Chem. Soc.*, 2009, **131**, 3152–3153.
10 X. Chen and S. S. Mao, *Chem. Rev.*, 2007, **107**, 2891–2959.
11 J. Joo, S. G. Kwon, T. Yu, M. Cho, J. Lee, J. Yoon and T. Hyeon, *J. Phys. Chem. B*, 2005, **109**, 15297–15302.
12 J. E. G. J. Wijnhoven and W. L. Vos, *Science*, 1998, **281**, 802.
13 C. J. Barbé, F. Arendse, P. Comte, M. Jirousek, F. Lenzmann, V. Shklover and M. Grätzel, *J. Am. Ceram. Soc.*, 1997, **80**, 3157–3171.
14 J. Tang, J. R. Durrant and D. R. Klug, *J. Am. Chem. Soc.*, 2008, **130**, 13885–13891.
15 H. Park, C. D. Vecitis, W. Choi, O. Weres and M. R. Hoffmann, *J. Phys. Chem. C*, 2008, **112**, 885–889.
16 R. Joy and S. Haridas, *Int. J. Hydrogen Energy*, 2021, **46**, 1879–1903.
17 M. Moniruddin, B. Ilyassov, X. Zhao, E. Smith, T. Serikov, N. Ibrayev, R. Asmatulu and N. Nuraje, *Materials Today Energy*, 2018, **7**, 246–259.
18 Y. Huang, J. Liu, Y. Deng, Y. Qian, X. Jia, M. Ma, C. Yang, K. Liu, Z. Wang, S. Qu and Z. Wang, *J. Semicond.*, 2020, **41**, 011701.
19 G. Canu and V. Buscaglia, *CrystEngComm*, 2017, **19**, 3867–3891.
20 B. L. Phoon, C. W. Lai, J. C. Juan, P.-L. Show and G.-T. Pan, *Int. J. Hydrogen Energy*, 2019, **44**, 14316–14340.
21 J.-i. Fujisawa, T. Eda and M. Hanaya, *Chem. Phys. Lett.*, 2017, **685**, 23–26.
22 E. Rocha-Rangel, W. J. Pech-Rodríguez, J. López-Hernández, C. A. Calles-Arriaga, E. N. Armendáriz-Mireles, J. A. Castillo-Robles and J. A. Rodríguez-García, *Arch. Metall. Mater.*, 2020, **65**, 621–626.
23 L. C. Yan, J. Hassan, M. Hashim, W. S. Yin, T. F. Khoon and W. Y. Jeng, *World Appl. Sci. J.*, 2011, **15**, 1614–1618.
24 L. Amaral, A. M. Senos and P. M. Vilarinho, *Mater. Res. Bull.*, 2009, **44**, 263–270.
25 P. Visuttipitukul, P. Sooksaen and N. Yongvanich, *Ferroelectrics*, 2013, **457**, 82–88.
26 P. Panthong, T. Klaytae, K. Boonma and S. Thountom, *Ferroelectrics*, 2013, **455**, 29–34.
27 W.-F. Zhang, Q. Xing and Y.-B. Huang, *Mod. Phys. Lett. B*, 2000, **14**, 709–716.
28 P. Balaya, M. Ahrens, L. Kienle, J. Maier, B. Rahmati, S. B. Lee, W. Sigle, A. Pashkin, C. Kuntscher and M. Dressel, *J. Am. Ceram. Soc.*, 2006, **89**, 2804–2811.
29 P. K. Roy and J. Bera, *Mater. Res. Bull.*, 2005, **40**, 599–604.
30 A. Shkabko, M. H. Aguirre, I. Marozau, M. Doebeli, M. Mallepell, T. Lippert and A. Weidenkaff, *Mater. Chem. Phys.*, 2009, **115**, 86–92.
31 C. N. George, J. Thomas, R. Jose, H. P. Kumar, M. Suresh, V. R. Kumar, P. S. Wariar and J. Koshy, *J. Alloys Compd.*, 2009, **486**, 711–715.
32 S. Liu, Z. Xiu, J. a. Liu, F. Xu, W. Yu, J. Yu and G. Feng, *J. Alloys Compd.*, 2008, **457**, L12–L14.
33 H. Ishikawa, K. Oohira, T. Nakajima and T. Akiyama, *J. Alloys Compd.*, 2008, **454**, 384–388.
34 B. L. Phoon, C. W. Lai, G.-T. Pan, T. C. K. Yang and J. C. Juan, *Ceram. Int.*, 2018, **44**, 9923–9933.
35 K. Nakashima, M. Kera, I. Fujii and S. Wada, *Ceram. Int.*, 2013, **39**, 3231–3234.
36 X. Wei, G. Xu, Z. Ren, Y. Wang, G. Shen and G. Han, *J. Am. Ceram. Soc.*, 2008, **91**, 299–302.
37 X. Wei, G. Xu, Z. Ren, C. Xu, G. Shen and G. Han, *J. Am. Ceram. Soc.*, 2008, **91**, 3795–3799.
38 V. Kalyani, B. S. Vasile, A. Ianculescu, M. T. Buscaglia, V. Buscaglia and P. Nanni, *Cryst. Growth Des.*, 2012, **12**, 4450–4456.
39 D. Chen, X. Jiao and M. Zhang, *J. Eur. Ceram. Soc.*, 2000, **20**, 1261–1265.
40 P. Jayabal, V. Sasirekha, J. Mayandi, K. Jeganathan and V. Ramakrishnan, *J. Alloys Compd.*, 2014, **586**, 456–461.
41 H.-D. Kurland, J. Grabow and F. A. Müller, *J. Eur. Ceram. Soc.*, 2011, **31**, 2559–2568.
42 C. Stötzel, H.-D. Kurland, J. Grabow, S. Dutz, E. Müller, M. Sierka and F. A. Müller, *Cryst. Growth Des.*, 2013, **13**, 4868–4876.

43 H.-D. Kurland, C. Stötzel, J. Grabow, I. Zink, E. Müller, G. Staupendahl and F. A. Müller, *J. Am. Ceram. Soc.*, 2010, **93**, 1282–1289.
44 H.-D. Kurland, J. Grabow, C. Stoetzel and F. Müller, *J. Ceram. Sci. Technol.*, 2014, **5**, 275–280.
45 C. Zollfrank, S. Gruber, M. Batentschuk, A. Osvet, F. Goetz-Neunhoeffer, S. Dittrich, J. Grabow, H.-D. Kurland and F. Müller, *Acta Mater.*, 2013, **61**, 7133–7141.
46 H.-D. Kurland, J. Grabow, G. Staupendahl, F. A. Müller, E. Müller, S. Dutz and M. E. Bellemann, *J. Magn. Magn. Mater.*, 2009, **321**, 1381–1385.
47 H. D. Kurland, C. Stotzel, J. Grabow, I. Zink, E. Muller, G. Staupendahl and F. A. Muller, *J. Am. Ceram. Soc.*, 2010, **93**, 1282–1289.
48 L. B. Tasyurek, M. Sevim, Z. Caldiran, S. Aydogan and O. Metin, *Mater. Res. Express*, 2018, **5**, 015060.
49 U. Holzwarth and N. Gibson, *Nat. Nanotechnol.*, 2011, **6**, 534.
50 J. I. Langford and A. J. C. Wilson, *J. Appl. Crystallogr.*, 1978, **11**, 102–113.
51 H. P. Klug and L. E. Alexander, *X-ray Diffraction Procedures: for Polycrystalline and Amorphous Materials*, 1974.
52 L. F. da Silva, O. F. Lopes, V. R. de Mendonça, K. T. G. Carvalho, E. Longo, C. Ribeiro and V. R. Mastelaro, *Photochem. Photobiol.*, 2016, **92**, 371–378.
53 L. F. da Silva, M. I. B. Bernardi, L. J. Q. Maia, G. J. M. Frigo and V. R. Mastelaro, *J. Therm. Anal. Calorim.*, 2009, **97**, 173.
54 Y. Sun, T. Hu, W. Zhang and X. Chen, *J. Adv. Oxid. Technol.*, 2017, **20**(1), 20160194.
55 M. Johnson, M. Ates, Z. Arslan, I. Farah and C. Bogatu, *J. Nanomed. Nanotechnol.*, 2017, **2**, 11–27.
56 F. A. Rabuffetti, P. C. Stair and K. R. Poeppelmeier, *J. Phys. Chem. C*, 2010, **114**, 11056–11067.
57 T. Mahalingam, C. Selvakumar, E. Ranjith Kumar and T. Venkatachalam, *Phys. Lett. A*, 2017, **381**, 1815–1819.
58 Z. Asgari-Fard, M. Sabet and M. Salavati-Niasari, *High Temp. Mater. Processes*, 2016, **35**, 215–220.
59 F. Azough, A. Gholinia, D. T. Alvarez-Ruiz, E. Duran, D. M. Kepaptsoglou, A. S. Eggeman, Q. M. Ramasse and R. Freer, *ACS Appl. Mater. Interfaces*, 2019, **11**, 32833–32843.
60 X. Zhu, J. Zhu, S. Zhou, Z. Liu, N. Ming and D. Hesse, *J. Cryst. Growth*, 2005, **283**, 553–562.
61 I. J. Clark, T. Takeuchi, N. Ohtori and D. C. Sinclair, *J. Mater. Chem.*, 1999, **9**, 83–91.
62 J. O. Eckert Jr., C. C. Hung-Houston, B. L. Gersten, M. M. Lencka and R. E. Riman, *J. Am. Ceram. Soc.*, 1996, **79**, 2929–2939.
63 H. Ohta, K. Sugiura and K. Koumoto, *Inorg. Chem.*, 2008, **47**, 8429–8436.
64 A. M. Schultz, T. D. Brown and P. R. Ohodnicki, *J. Phys. Chem. C*, 2015, **119**, 6211–6220.
65 *Ternary Compounds, Organic Semiconductors*, ed. O. Madelung, U. Rössler and M. Schulz, Springer-Verlag Berlin Heidelberg, 2000, ch. 531, pp. 1–3.
66 *II-VI and I-VII Compounds; Semimagnetic Compounds*, ed. O. Madelung, U. Rössler and M. Schulz, Springer-Verlag Berlin Heidelberg, 1999, ch. 245, pp. 1–3.
67 P. Nyamukamba, O. Okoh, H. Heroe, R. Taziwa and S. Zinya, Synthetic Methods for Titanium Dioxide Nanoparticles: A Review, in *Titanium Dioxide - Material for a Sustainable Enviroment*, ed. D. Yang, IntechOpen, London, 2018, ISBN: 978-1-78923-327-8.
68 E. Bagherisereshki, J. Tran, F. Lei and N. AuYeung, *Solar Energy*, 2018, **160**, 85–93.
69 R. Hooley, A. Brown and R. Brydson, *Micron*, 2019, **120**, 25–34.
70 N. Jiang, *Rep. Prog. Phys.*, 2016, **79**, 3–33.
71 M. Ullmann, S. K. Friedlander and A. Schmidt-Ott, *J. Nanopart. Res.*, 2002, **4**, 499–509.
72 M. Hütter, *J. Non-Newtonian Fluid Mech.*, 2004, **120**, 55–68.
73 O. V. Oyelade, O. K. Oyewole, D. O. Oyewole, S. A. Adeniji, R. Ichwani, D. M. Sanni and W. O. Soboyejo, *Sci. Rep.*, 2020, **10**, 7183.
74 A. Matthews, *Am. Mineral.*, 1976, **61**, 419–424.
75 P.-T. Hsiao, M.-D. Lu, Y.-L. Tung and H. Teng, *J. Phys. Chem. C*, 2010, **114**, 15625–15632.
76 Y. Song, T. Liu, B. Yao, M. Li, T. Kou, Z.-H. Huang, D.-Y. Feng, F. Wang, Y. Tong, X.-X. Liu and Y. Li, *ACS Energy Lett.*, 2017, **2**, 1752–1759.
77 B. Liu and H. C. Zeng, *Small*, 2005, **1**, 566–571.
78 C. C. Yec and H. C. Zeng, *J. Mater. Chem. A*, 2014, **2**, 4843–4851.